Optics Communications 574 (2025) 131203

Contents lists available at ScienceDirect

Optics Communications

journal homepage: www.elsevier.com/locate/optcom

Talbot-effect-based multiplication of Laguerre–Gaussian beams with non-zero radial indices: From theory to experimental realization

Pouria Amiri [a], Saifollah Rasouli [a,b,c,*], Davud Hebri [d], Sergey A. Ponomarenko [d,e]

[a] Department of Physics, Institute for Advanced Studies in Basic Sciences (IASBS), Zanjan 45137-66731, Iran
[b] Center for International Scientific Studies and Collaboration (CISSC), Ministry of Science, Research and Technology, Tehran 15875-7788, Iran
[c] Optics Research Center, Institute for Advanced Studies in Basic Sciences (IASBS), Zanjan 45137-66731, Iran
[d] Department of Physics and Atmospheric Science, Dalhousie University, Halifax, Nova, Scotia B3H 4R2, Canada
[e] Department of Electrical and Computer Engineering, Dalhousie University, Halifax, Nova, Scotia B3J 2X4, Canada

ARTICLE INFO

Keywords:
Talbot effect
beams
Two-dimensional (2D) periodic structures
Multiplexed LG modes

ABSTRACT

We present a Talbot self-imaging inspired method for multiplying Laguerre–Gaussian (LG) beams of non-zero radial indices. We explore theoretically and experimentally the LG beam diffraction from two-dimensional (2D) periodic structures. In particular, we determine near-field LG beam diffraction patterns from a 2D binary grating of a small opening ratio (OR). We demonstrate that incident LG beam intensity patterns are reproduced as images of individual square apertures of the grating in certain Talbot planes. We also investigate the impact of the number of fractional-Talbot and Talbot planes on the quality of the generated 2D array of multiplexed LG modes. Our theoretical predictions are in good agreement with our experiments. Our method can find applications in optical communication, optical tweezing, multi-particle trapping, screening, and micro-manipulation.

1. Introduction

The generation and characterization of optical vortex lattices (OVLs) have piqued the interest to researchers primarily due to such applications of vortex beams (VBs) as optical tweezing [1–4], optical processing [5], particle trapping and guiding [6,7], and optical communications [8,9]. Numerous diffraction and interference-based methods have been advanced to generate OVLs with the aid of Dammann gratings [10] and spatial light modulators (SLMs) [8,11]. Some recent SLM inspired approaches include phase multiplication and arbitrary mode control [12], transformation optics [13], and adaptive generation of complex light arrays [14]. Additionally, the wavefront of the beam can be precisely shaped using an axicon array [15] and a spiral phase array [16]. These methods are pivotal in the generation of a two-dimensional (2D) array of vortex beams. Vortex light interference is another alternative for generating an OVL. For instance, Laguerre–Gaussian (LG) beams [17], Bessel beams [18], and perfect OVs [19] have already been used to generate OVLs. Further, optical coherence lattices [20–22] have been successfully employed to generate arrays of partially coherent Bessel beams carrying optical vortices [23], as well as polarization arrays [24].

Yet another method of generating an OVL utilizes the Talbot effect with a VB illumination of a 2D grating. In [17] the authors developed a theory of diffraction of LG beams with zero radial index from 2D periodic structures. In particular, they have shown that a zero radial index LG with an odd topological charge (TC) diffracted from a 2D sinusoidal or Ronchi grating can be multiplexed into an LG array at the Talbot planes of the structure, so that all multiplexed LGs carry a unit TC. However, it was shown in [25] that as long as the opening ratio (OR) of the grating is much smaller than 1/2, the multiplexed arrays carry the same TC as the source LG beam regardless of the magnitude and parity of its TC. Experimental generation of OVLs with the aid of the Talbot phenomenon under illumination with VBs having zero radial index have also been reported [26–29]. We note in passing that in [30–32], the diffraction of an LG beam with zero radial index from a one-dimensional (1D) grating was successfully utilized to determine the TC of an incident vortex beam. Further, it was shown in [33] that for a 1D grating with a much smaller OR, the contrast of the fringe-like diffraction pattern formed at the image location of individual lines of the grating increases significantly.

At the same time, the diffraction of a VB with non-zero radial index from a 1D grating with a small OR has also been recently studied [34], and in this diffraction geometry, the transformation of LG beams into a 1D array of Hermite–Gaussian modes was reported. It is also worth noting that the Talbot self-imaging of a linear grating, illuminating

* Corresponding author at: Department of Physics, Institute for Advanced Studies in Basic Sciences (IASBS), Zanjan 45137-66731, Iran.
E-mail address: rasouli@iasbs.ac.ir (S. Rasouli).

https://doi.org/10.1016/j.optcom.2024.131203
Received 1 August 2024; Received in revised form 23 September 2024; Accepted 11 October 2024
Available online 18 October 2024

by a VB, into another similar linear grating in a moiré deflectometry setup was used for the illuminating beam characterization [35], and the same arrangement was utilized to detect a TC sign change on reflection in [36].

In this work, we explore the multiplication of LG beams with non-zero radial indices using the Talbot effect. We demonstrate the generation of multiple copies of an incident LG beam with arbitrary TC in specific Talbot planes of a 2D binary grating with small OR by illuminating the grating with an LG beam with a non-zero radial index. We optimize the quality of generated LG arrays by identifying the optimum Talbot planes for high-quality optical OVL production using a degree of similarity. We successfully verify our analytical theory with experiments. Our approach is simpler and more cost-effective than any SLM-based method. Unlike interference-based methods, our protocol enables generation of a large number of vortices at a given Talbot plane, which are then replicated during propagation. This approach holds promise for applications to optical communications, optical tweezing, lensless multi-particle trapping, screening, and micro-manipulation.

It is important to highlight the new features of this work compared to the method presented in [25]. In [25], only the theory of diffraction of an LG beam with a given value of l and a zero radial index ($p = 0$) was presented. In the general case of $p \neq 0$, treated here, the conditions for generating arrays of LG beams at specific Talbot distances depend on p, which was not addressed in the previous method. Since LG beams with $p \neq 0$ have multiple intensity rings, we evaluate the resulting beams by comparing them to the corresponding ideal LG ones. Additionally, this work presents, for the first time to our knowledge, experimental results on the generation of arrays of LG beams with $p \neq 0$ based on the Talbot effect. Previous studies, such as [17,25], only considered theoretical conditions for incident beams with $p = 0$ and impinging structures with various OR. Furthermore, this work details how to produce high radial index LG beams using multi-circle phase-shifted amplitude fork gratings. Finally, in this work we explore in greater detail how the results can be implemented in multi-particle trapping, manipulation, and optical communications.

2. Diffraction of optical beams from 2D orthogonal periodic structures: a general formulation

Let Λ_x and Λ_y be fundamental periods and $f_x = \Lambda_x^{-1}$ and $f_y = \Lambda_y^{-1}$ be fundamental frequencies of a 2D orthogonal periodic structure along x and y directions, respectively. The transmittance of light through the structure can be expressed as a 2D Fourier series as [37,38]:

$$t(\mathbf{r}) = \sum_{m,n=-\infty}^{+\infty} t_{m,n} e^{i\mathbf{k}_{m,n}\cdot\mathbf{r}}, \tag{1}$$

where $\mathbf{r} = (x, y) = (r\cos\theta, r\sin\theta)$ is a position vector, $\mathbf{k}_{m,n} = (2\pi m f_x, 2\pi n f_y)$, and $t_{m,n}$ indicates the (m,n)th Fourier coefficient. Now assume that the 2D orthogonal periodic structure is illuminated by an optical beam with a finite transverse extent. The complex field $\Psi(\mathbf{r}, 0)$ of the beam immediately past the structure is related to the incident field $u(\mathbf{r}, 0)$ by the expression

$$\Psi(\mathbf{r}, 0) = t(\mathbf{r}) u(\mathbf{r}, 0). \tag{2}$$

Next, the field, having propagated over a distance z in free space away from the structure, can be expressed as [38]

$$\Psi(\mathbf{r}, z) = \left(\frac{k}{2\pi i z}\right) \int d\mathbf{r}' \Psi(\mathbf{r}', 0) e^{ik(\mathbf{r}'-\mathbf{r})^2/(2z)}, \tag{3}$$

where $k = 2\pi/\lambda$, λ being a carrier wavelength. On substituting for $t(\mathbf{r})$ from Eqs. (1) and (2) into Eq. (3) and re-arranging exponential terms, we obtain

$$\Psi(\mathbf{r}, z) \propto \sum_{m,n=-\infty}^{+\infty} t_{m,n} e^{-ikr_{m,n}^2/(2z)} \left(\frac{k}{2\pi i z}\right) \int d\mathbf{r}' u(\mathbf{r}', 0) e^{ik(\mathbf{r}'-\mathbf{r}_{m,n})^2/(2z)}. \tag{4}$$

Here $\mathbf{r}_{m,n} = \mathbf{r} - \mathbf{k}_{m,n} z/k$ where $\mathbf{k}_{m,n} z/k$ is a position vector of the center of the (m,n)th diffraction order so that $\mathbf{r}_{m,n}$ can be regarded as the position vector in the coordinates transformed to the center of the (m,n)th diffraction order and we dropped an irrelevant overall quadratic phase factor. Observing that the inner integral on the right-hand side of Eq. (4), together with the factor $k/2\pi i z$, yields the incident field propagated to the plane $z = const \geq 0$, we can rewrite Eq. (4) as

$$\Psi(\mathbf{r}, z) \propto \sum_{m,n=-\infty}^{+\infty} t_{m,n} e^{-ikr_{m,n}^2/(2z)} u\left(\mathbf{r}_{m,n}, z\right), \tag{5}$$

where $\mathbf{r}_{m,n} = (x_m, y_n) = (x - m\lambda z f_x, y - n\lambda z f_y)$. We note in passing that this result can alternatively be derived following the approach of [34].

We now specify to incident LG beams defined as [39]:

$$u(\mathbf{r}, 0) \propto \left(\frac{x + isy}{w_0}\right)^{|l|} \exp\left(-\frac{r^2}{w_0^2}\right) L_p^{|l|}\left(\frac{2r^2}{w_0^2}\right), \tag{6}$$

where l and w_0 denote the TC and width of a beam, respectively. The TC sign is determined by s and $L_P^{|l|}$ denotes an associated Laguerre polynomial, where p shows the radial index of the beam. The complex amplitude of an LG beam at the propagation distance z away from the source can be expressed as

$$u(\mathbf{r}, z) \propto g_p^l(z) \left(\frac{x + isy}{w(z)}\right)^{|l|} \exp\left(\frac{ikr^2}{2q(z)}\right) L_p^{|l|}\left[\frac{2r^2}{w^2(z)}\right], \tag{7}$$

where

$$g_p^l(z) = \frac{w_0}{w(z)} \exp\left[ikz - i\left(|l| + 2p + 1\right)\zeta(z)\right], \tag{8}$$

and

$$\frac{1}{q(z)} = \frac{1}{R(z)} + i\frac{\lambda}{\pi w^2(z)}. \tag{9}$$

In Eqs. (7) through (9), we introduced the following definitions:

$$w(z) = w_0\sqrt{1 + \left(\frac{z}{z_0}\right)^2}, \tag{10a}$$

$$R(z) = z\left[1 + \left(\frac{z_0}{z}\right)^2\right], \tag{10b}$$

$$\zeta(z) = \tan^{-1}\left(\frac{z}{z_0}\right), \tag{10c}$$

where $w(z)$ is a current beam width, $\zeta(z)$ denotes a Gouy phase shift, and z_0 stands for a Rayleigh range given by $z_0 = \frac{\pi w_0^2}{\lambda}$.

For the sake of illustration, we display the intensity and phase patterns of an LG beam with $l = 3$, $p = 1$ in Fig. 1(a) and (b). We can trivially convert the amplitude and intensity to polar coordinates to yield the results in Eqs. (A.1) and (A.2) of Appendix A. As shown in the Appendix, the intensity is a function of a dimensionless radial parameter, denoted by $R = \frac{r}{w_0}$. We depict the radial intensity distribution of LG beam with $l = 3$, $p = 1$ in Fig. 1(c). Next, we can define two radial parameters r_{in} and r_{out} as the nearest and farthest radial distances from the optical axis at which the intensity falls to $\frac{1}{10}$ of the maximum intensity, respectively. The corresponding dimensionless parameters $R_{\text{in}} = \frac{r_{\text{in}}}{w_0}$ and $R_{\text{out}} = \frac{r_{\text{out}}}{w_0}$ can be evaluated in terms of l and p, and we show them in Fig. 1(d) and (e).

Now suppose that a 2D orthogonal periodic structure, with a transmittance indicated by Eq. (1), is illuminated by an LG beam at its beam waist shown by Eq. (6). It follows at once by combining Eqs. (5) and (7) that

$$\Psi(\mathbf{r}, z) \propto g_p^l(z) \sum_{m,n=-\infty}^{+\infty} t_{m,n} e^{-ikr_{m,n}^2/(2z)} \left(\frac{x_m + isy_n}{w(z)}\right)^{|l|} \times \exp\left(\frac{ikr_{m,n}^2}{2q(z)}\right) L_p^{|l|}\left(\frac{2r_{m,n}^2}{w^2(z)}\right). \tag{11}$$

Eq. (11) yields a general expression for the optical field of an LG beam diffracted from a 2D orthogonal periodic structure of arbitrary profile.

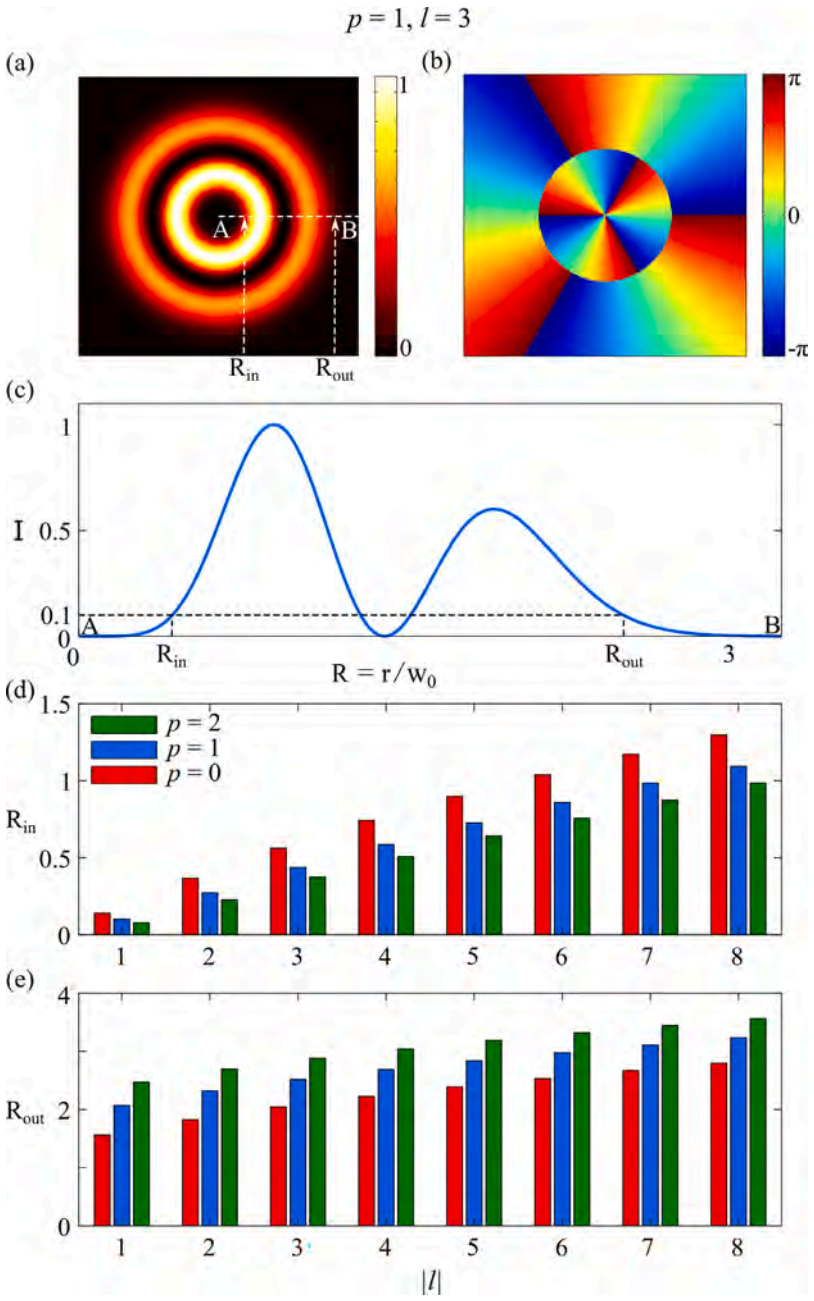

Fig. 1. (a) Intensity and (b) phase patterns of an LG beam with $l = 3$, $p = 1$. (c) The intensity profile along the radial direction is illustrated in (a) with the dashed line AB. (d) and (e), R_{in} and R_{out} of different LG beams having different values of TC and radial index.

3. LG beam multiplication

We are now in a position to examine the diffraction of an LG beam with non-zero radial index from a 2D orthogonal binary grating with the transmission function

$$t(x,y) = \frac{1}{4}\left\{1 + \text{sign}\left[\cos\left(\frac{2\pi x}{\Lambda}\right) - \cos(\pi\mu)\right]\right\} \times \left\{1 + \text{sign}\left[\cos\left(\frac{2\pi y}{\Lambda}\right) - \cos(\pi\mu)\right]\right\}, \quad (12)$$

where "sign" denotes a signum function, Λ is a period of the grating in both x and y directions, namely $\Lambda_x = \Lambda_y = \Lambda$, and $\mu = \frac{a}{\Lambda}$ is the OR. The signum function simply gives the sign for the given values of its argument. For argument value greater than zero, the value of the output is +1, for argument value lesser than zero, the value of the output is −1, and for zero value of argument, the value of the output is zero. The parameter μ in the equation ranges from 0 to 1 and acts as the OR of the resulted binary grating. By changing the value of μ in the transmission function $t(x, y)$, we directly alter the OR of the binary grating. As μ increases, the width a of the open regions increases proportionally, thereby increasing the OR. Conversely, decreasing μ reduces the width a of the open regions, thus decreasing the OR. This relationship ensures that the OR is always equal to the value of μ used in the equation, and it changes linearly with μ. The grating is schematically depicted in Fig. 1 of Ref. [25] and the corresponding Fourier coefficients, $t_{m,n}$, are given by Eq. (21) of the same reference. We can then evaluate the diffracted light field by substituting said coefficients into Eq. (11).

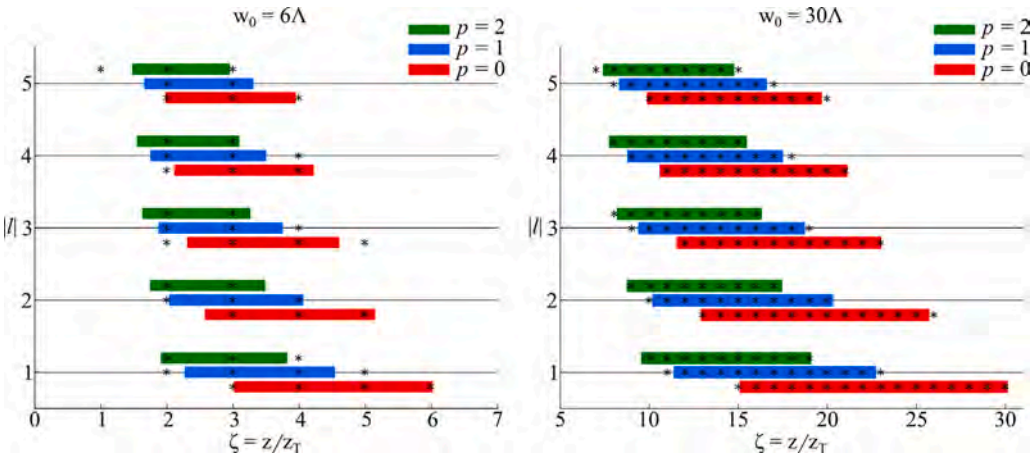

Fig. 2. Colored horizontal bars show multiplication intervals for different values of TC and radial index at $w_0 = 6\Lambda, 30\Lambda$. Stars show the locations of optimal Talbot planes within multiplication intervals or the closest to their endpoints. See also Visualization 1.

3.1. Conditions for LG beam multiplication

In Ref. [17], the diffraction pattern of LG beams of zero radial index, $p = 0$, by a 2D periodic sinusoidal grating was examined and the optimal self-healing position and interval behind the grating were determined. It was shown that the former is given by $z_1 \approx \frac{\Lambda}{\lambda} w_{\text{eff}}$, where Λ is a grating period, and $w_{\text{eff}} = w_0\sqrt{\frac{|l|}{2}}$ is an effective radius of the LG beam. As only first diffraction orders are present in this case, their interference generates a 2D array of LG beams with TC = 1 whenever l is odd, and TC = 0 for even l's. We refer to this phenomenon as the first diffraction order interference (FDOI) effect in [25], where a multiplication interval, describing the propagation distance over which the VB multiplication occurs, is also determined. To obtain multiple replicas of an incident LG beam carrying any TC, the interference of higher diffraction orders must be present.

We now adopt the approach of Ref. [25] to figure out the optimal Talbot plane positions and multiplication interval to multiply LG beams with non-zero radial index diffracted by the same type of grating with small OR. To this end, we estimate the spatial frequency extent of the incident LG beam in Appendix A. Using Eq. (A7) in Eq. (13) of [25], we obtain for the sought interval, normalized to z_T, the following expression:

$$\frac{\pi w_0}{4\Lambda R_{\text{out}}} < \zeta < \frac{\pi w_0}{2\Lambda R_{\text{out}}}. \tag{13}$$

We exhibit the dimensionless parameter r_{out} in Fig. 1(e) as a function of l and p. Eq. (13) identifies the Talbot plane positions within which we can attain the highest multiplication accuracy. We mark the locations of these optimal planes with stars in Fig. 2 and indicate ζ falling within the interval specified by Eg. (13) with colored horizontal bars corresponding to varied $|l|$, p, and $\frac{w_0}{\Lambda}$. In Fig. 2 we exhibit the results for $w_0 = 6\Lambda, 30\Lambda$, $|l| = 1, \ldots, 5$, and $p = 0, 1, 3$. As ζ is an integer, we use the nearest integer part function, $\lfloor\,\rfloor$, to find its minimum and maximum values as

$$\zeta_{\min} = \left\lfloor \frac{\pi w_0}{4\Lambda R_{\text{out}}} \right\rfloor, \tag{14a}$$

$$\zeta_{\max} = \left\lfloor \frac{\pi w_0}{2\Lambda R_{\text{out}}} \right\rfloor. \tag{14b}$$

These two equations define the closest and the most distant Talbot planes from the grating for which the optimal VB multiplication occurs. We refer to the distance between the two optimal planes as a multiplication interval. We can find the optimal propagation distance, $z_{\text{opt}} = \zeta_{\text{opt}} z_T$, by comparing the replicated versus the original LG beams and maximizing the similarity between the two. In the next section, we show that ζ_{opt} is close to the end of the multiplication interval using a similarity function.

Eqs. (13) and (14) imply that the boundaries and length of the multiplication interval are inversely proportional to R_{out}. However, by boosting the ratio of the beam waist to the grating period, $\frac{w_0}{\Lambda}$, the multiplication interval can be enlarged and its center shifted away from the grating. This is because the value of R_{out} increases with the magnitude of TC and radial index, see Fig. 1(e). By increasing $|l|$ and p, the length of the multiplication interval can be reduced, with its center shifting toward the diffraction grating. We illustrate these trends in Fig. 2. In the background Visualization 1, we exhibit the field patterns, evaluated in different Talbot planes, of LG beams with $l = 2$ and variable radial indices.

Fig. 2 illustrates a comparative analysis between two images, one with a width of ($w_0 = 6\lambda$) and the other with ($w_0 = 30\lambda$). This comparison highlights a quintuple proportionality between the dimensions of the two images.

As previously mentioned, 2D gratings with sinusoidal and Ronchi profiles are not suitable for generating replicas of the incident beam with topological values greater than one, ($l > 1$). This is due to the absence of higher-order diffraction by sinusoidal gratings and the elimination of even diffraction orders by Ronchi gratings. Consequently, the interference of these limited diffraction orders in the near field of these gratings produces an array of LG beams with $l = 1$ in the image planes for odd l, regardless of the l value of the incident LG beams. For even l, it produces self-images of the grating apertures [25]. To point out this issue, it is necessary to include other diffraction orders in the spectrum to contribute to the formation of the beam array. Diffraction of LG beams with arbitrary l and $p = 0$ from binary gratings with different ORs is studied in [25]. It has been shown that for the TC of the array elements to match the TC of the incident light, an OR of one-tenth is optimal. Therefore, in this work, we consistently use an OR of one-tenth for 2D structures.

4. Degree of similarity of generated and source LG beams

To determine the quality of a Talbot effect generated LG mode, we compare its intensity pattern, I' with that of the incident LG beam, I in the same transverse plane $z = \text{const}$. The complex amplitude of the latter is proportional to a scaled Fourier transform of the source, c.f. Ref. [25]. The Fourier transform of an LG mode in polar coordinates is given by Eq. (A.6). It follows that by setting $\rho = \frac{r}{\lambda z}$, $\rho_0 = \frac{1}{\pi w_0}$, and $\frac{\rho}{\rho_0} = \frac{\pi w_0}{\lambda z} r$ in Eq. (A.6), we can obtain the complex amplitude of the incident LG beam. By applying the Fourier transform to Eq. (7) with these parameters, we can re-scale the incident beam to facilitate comparison with the Talbot-generated LG mode.

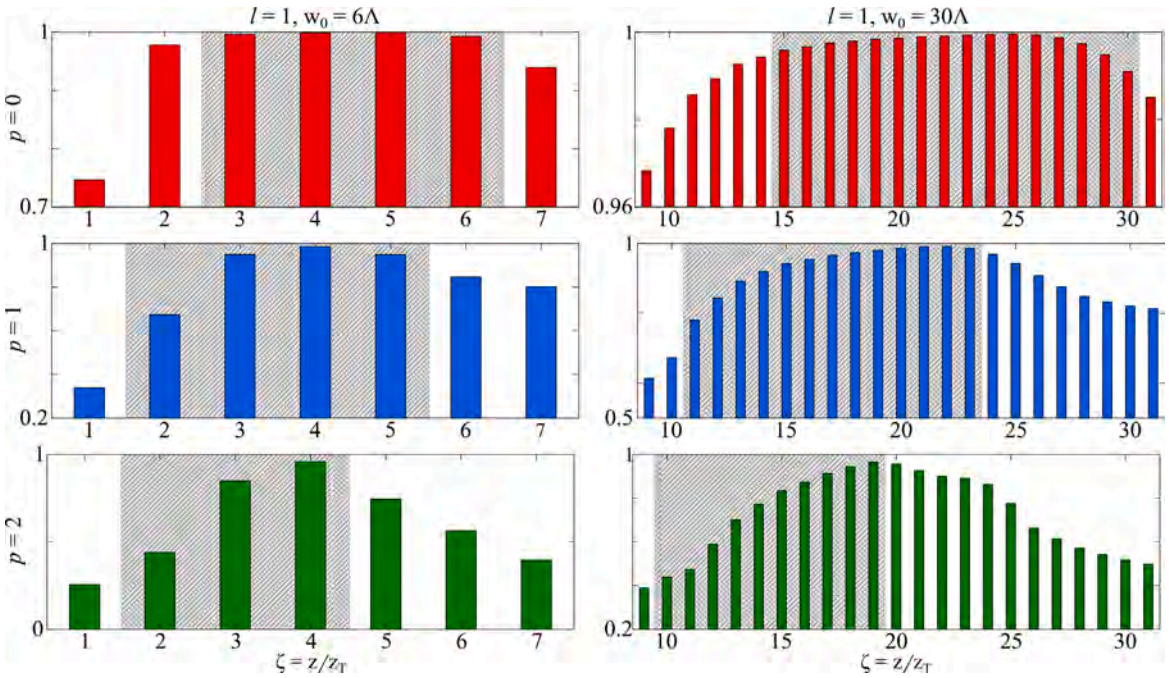

Fig. 3. Degree of similarity between the Talbot generated LG modes and the original LG beams with $l = 1$, and three radial indices for $w_0 = 6\Lambda, 30\Lambda$. In all plots, hatched lengths determine the corresponding $\zeta_{\min}$ to $\zeta_{\max}$ intervals.

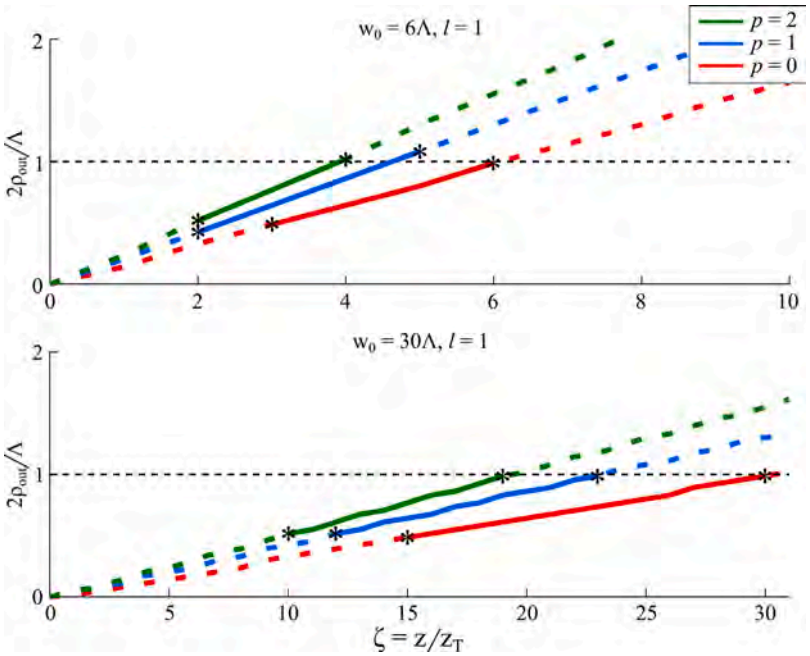

Fig. 4. $\frac{2\rho_{out}}{\Lambda}$ as a function of the propagation distance for variable w_0, l, and p. Stars show locations of the closest Talbot planes to endpoints of the multiplication interval, while continuous colored plots cover all Talbot planes with the highest multiplication accuracy.

We use the following degree of similarity to quantify the quality of the LG beam multiplication [40]:

$$S = \frac{\iint I(x,y)\, I'(x,y)\, dxdy}{\iint I^2(x,y)\, dxdy + \iint I'^2(x,y)\, dxdy - \iint I(x,y)\, I'(x,y)\, dxdy}, \quad (15)$$

In Fig. 3, we show the degree of similarity between the generated and incident LG beams propagated to the same transverse plane for $l = 1$ and $w = 6\Lambda, 30\Lambda$. The hatched areas in Fig. 3 indicate the optimal Talbot distances that cover a range between $\zeta_{\min}$ and $\zeta_{\max}$. As is seen in the figure for $p = 0$, the degree of similarity for the replicas in any Talbot plane within the interval $[\zeta_{\min}, \zeta_{\max}]$ is nearly unity. For higher values of p, since the intensity of the field inside the inner rings grows with the propagation distance, so does the degree of similarity. However, the adjacent LG modes start overlapping for sufficiently long propagation distances. For these reasons, the most optimal Talbot planes are located at the end of the multiplication interval (see Visualization 1).

We define an outer radius ρ_{out} of a replica beam as a distance from the center of the beam to the point where the intensity drops to $\frac{1}{10}$ of its maximum value. The outer radius grows with the propagation distance. An optimal replica beam will have a maximum size of a

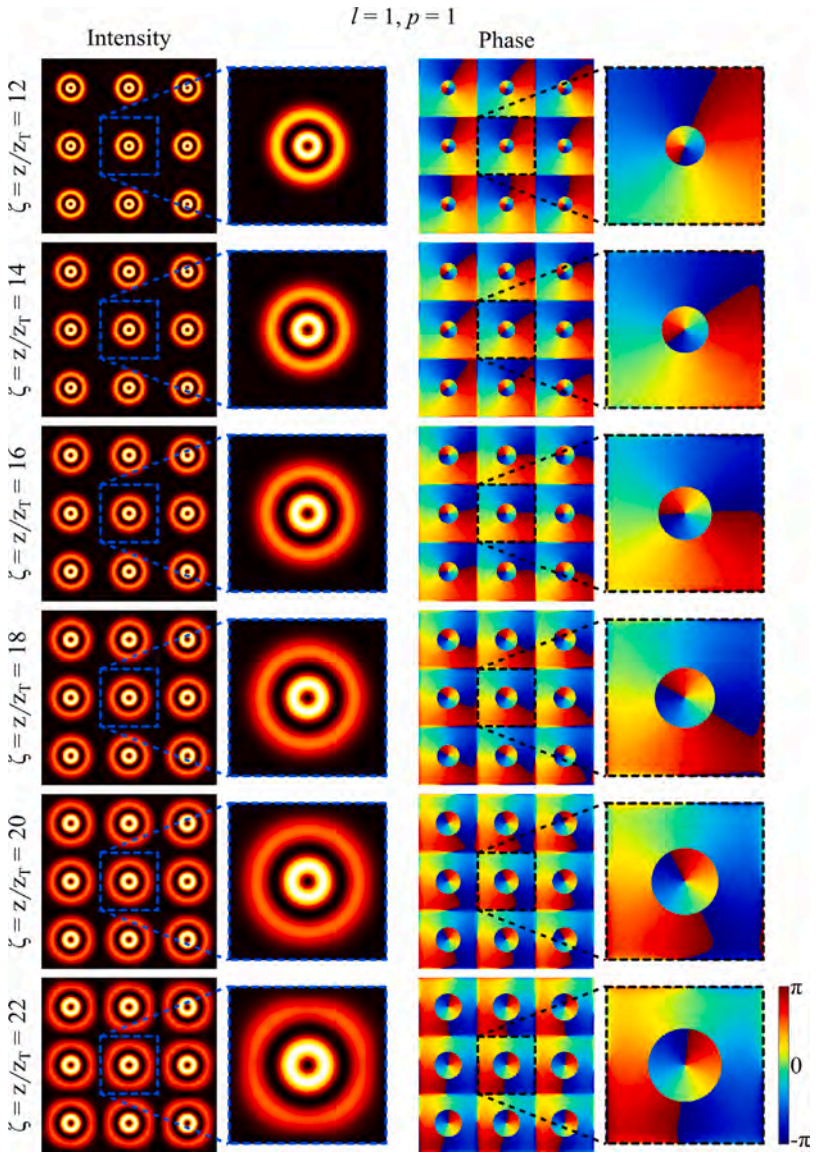

Fig. 5. Multiplication of an LG with $l = 1$, $p = 1$, $w_0 = 30\Lambda$, and $\lambda = 532$ nm facilitated by a binary grating with $\Lambda = 0.2$ mm and $\mu = 0.1$ in integer Talbot planes. The first column shows intensity profiles in a window encompassing the optical axis which is comprised of nine Talbot cells (an area of $3\Lambda \times 3\Lambda$); the second column shows intensity profiles over a single Talbot cell (an area of $\Lambda \times \Lambda$); third and fourth columns show the phase profiles corresponding to the first and second columns.

window with an area equal to the square of the grating period, Λ^2. This is because, as the replica beams spread on propagation they start overlapping which causes distortion over a certain propagation distance; this distortion reduces their similarity to the incident beam. Beyond this window, adjacent beams interfere with each other and their degree of similarity drops precipitously (see Visualization 1). We define an optimal propagation distance, ζ_{opt}, over which the replica and original beams maintain maximum similarity. As shown in Fig. 3, ζ_{opt} is always close to the end of the multiplication interval. We evaluate $\frac{2\rho_{out}}{\Lambda}$ as a function of the propagation distance varying w_0, l, p and present the results in Fig. 4. Stars show the Talbot planes located at the endpoints of intervals, say ζ_{min} and ζ_{max}. The ratio $\frac{2\rho_{out}}{\Lambda}$ increases linearly with distance and reaches unity at about the end of the interval. It follows that ζ_{opt} is located at that end. This conclusion reaffirms the results displayed in Fig. 3, indicating greater similarity toward the end of the multiplication interval, especially for higher values of the radial index.

We evaluate how closely the generated beams mimic the original beam, as illustrated in Fig. 3. The variations of the degree of similarities, marked by an initial rise followed by a decline, are indicative of the spatial dynamics of diffraction orders. Proximal to the grating, the diffraction orders are yet to coalesce, precluding substantial interference. In contrast, at extended distances, the diffraction orders diverge adequately, forestalling any interference. This dynamic accounts for the degree of similarities' ascent at lower z-coordinates, where convergence begins, and its descent as the orders separate, effectively minimizing crosstalk.

In Fig. 4, the curvature observed in the solid line of the lower image can be attributed to the limited spatial resolution of the simulation. This inherent constraint in the simulation's resolution results in a less precise representation of the expected linear trajectory, thereby manifesting as a noticeable curvature in the graphical output. It is important to note that this does not reflect an error in the underlying physical principles, but rather a limitation of the simulation's capacity to depict fine details at a higher resolution.

In Fig. 5, we illustrate the multiplication of a VB with $l = p = 1$, $w_0 = 30\Lambda$, and $\lambda = 532$ nm at integer Talbot planes of a binary grating with $\Lambda = 0.2$ mm and $\mu = 0.1$. The first column shows the evaluated intensity patterns on a window around optical axes consisting of nine Talbot cells (area of $3\Lambda \times 3\Lambda$). The second column exhibits the same patterns over one of the single Talbot cells (area of $\Lambda \times \Lambda$), and in the

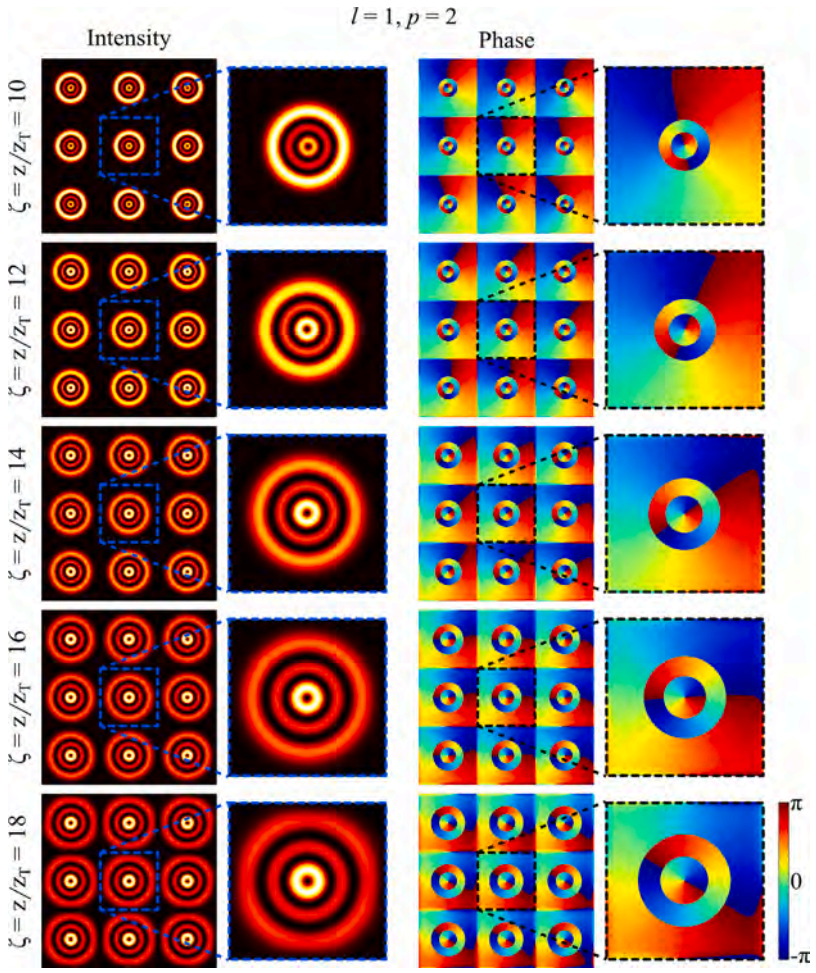

Fig. 6. Same patterns as those in Fig. 5 corresponding to $l = 1,\ p = 2$.

third and fourth columns, we present the corresponding phase profiles of the first and second columns.

In Fig. 6, we exhibit the patterns for $l = 1,\ p = 2$, which are similar to those of Fig. 5. Further, we show the multiplication of LG beams with variable TC and radial index at the optimal Talbot plane ζ_{opt} in Fig. 7. All parameters are the same as in Fig. 5. We also present additional details in the background of Visualization 1.

In Fig. 8, we display the intensity profiles of selected LG modes generated in Talbot planes of the same grating as in Fig. 5. We present intensity profiles along the dashed line on each individually generated pattern and those of the corresponding incident LG beams in the third, sixth, and ninth rows with solid and dashed lines, respectively. The maximal similarity is attained in the intermediate Talbot planes. Such a behavior is also manifest in Fig. 3.

Now, let us delve into the details of the formation of LG beam arrays in fractional Talbot planes. Fig. 9 illustrates the intensity and phase patterns observed in front of the nine central apertures of the grating under LG beam illumination with $l = 1$ and $p = 0$. These patterns are captured at various Talbot distances. In full Talbot planes ($z = 2z_T$ and $z = 4z_T$, where we use $z_T = \frac{\Lambda^2}{\lambda}$), the same array of the incident LG beam is formed in front of the grating apertures. In half-Talbot planes ($z = z_T$ and $z = 3z_T$), there is a half-period shift in both the x and y directions. In the quarter-Talbot planes ($z = 0.5z_T$, $z = 1.5z_T$, $z = 2.5z_T$, and $z = 3.5z_T$), we observe a duplication in the frequency of the generated arrays. Similarly, in octant Talbot planes ($z = 0.25z_T$, $z = 0.75z_T$, $z = 1.25z_T$, $z = 1.75z_T$, $z = 2.25z_T$, $z = 2.75z_T$, $z = 3.25z_T$, and $z = 3.75z_T$), there is another duplication of the arrays with respect to the quarter-Talbot planes. The first and second row insets show enlarged regeneration of the incident LG beam in front of each aperture. As is seen in the figures, the quality of the generated quarter and octant Talbot images decreases over longer propagation distances. This phenomenon is due to the increased size of the replicated LG beam over long propagation distances. In the quarter and octant Talbot planes, the number of array members in each direction is two and four times greater than that in the Talbot and half-Talbot planes, respectively. As the propagation distance increases, the LG beam replicas expand in te transverse plane and overlap with each other losing their structure. Other parameters for the beam and grating are the same as in Fig. 5.

We turn our attention to the same scenario as in Fig. 9, but under LG beam illumination with $l = 1$ and $p = 1$. Fig. 10 illustrates the corresponding intensity and phase patterns observed in front of the nine central apertures of the grating at the Talbot, half-Talbot, quarter Talbot, and octant Talbot distances. Since the incident beam has two intensity rings and its dimensions are larger than those in Fig. 9, the replicas of the incident beam in the quarter and octant-Talbot planes cannot be separated from each other, even at shorter propagation distances, resulting in transverse overlap. This overlap prevents the formation of distinct beam arrays at these distances.

Now let us show that how we can position the proposed method of generating arrays of LG beams as a very promising method for alternative use in optical communications and optical tweezing. To address the resulting beams evaluation further, we clarify that the phase profiles of the generated arrays demonstrate that each element possesses the expected orbital angular momentum (OAM). These phase profiles confirm OAM content of each generated LG beam.

By demonstrating the feasibility of generating structured beam arrays without the use of SLMs or intricate optical systems, our approach

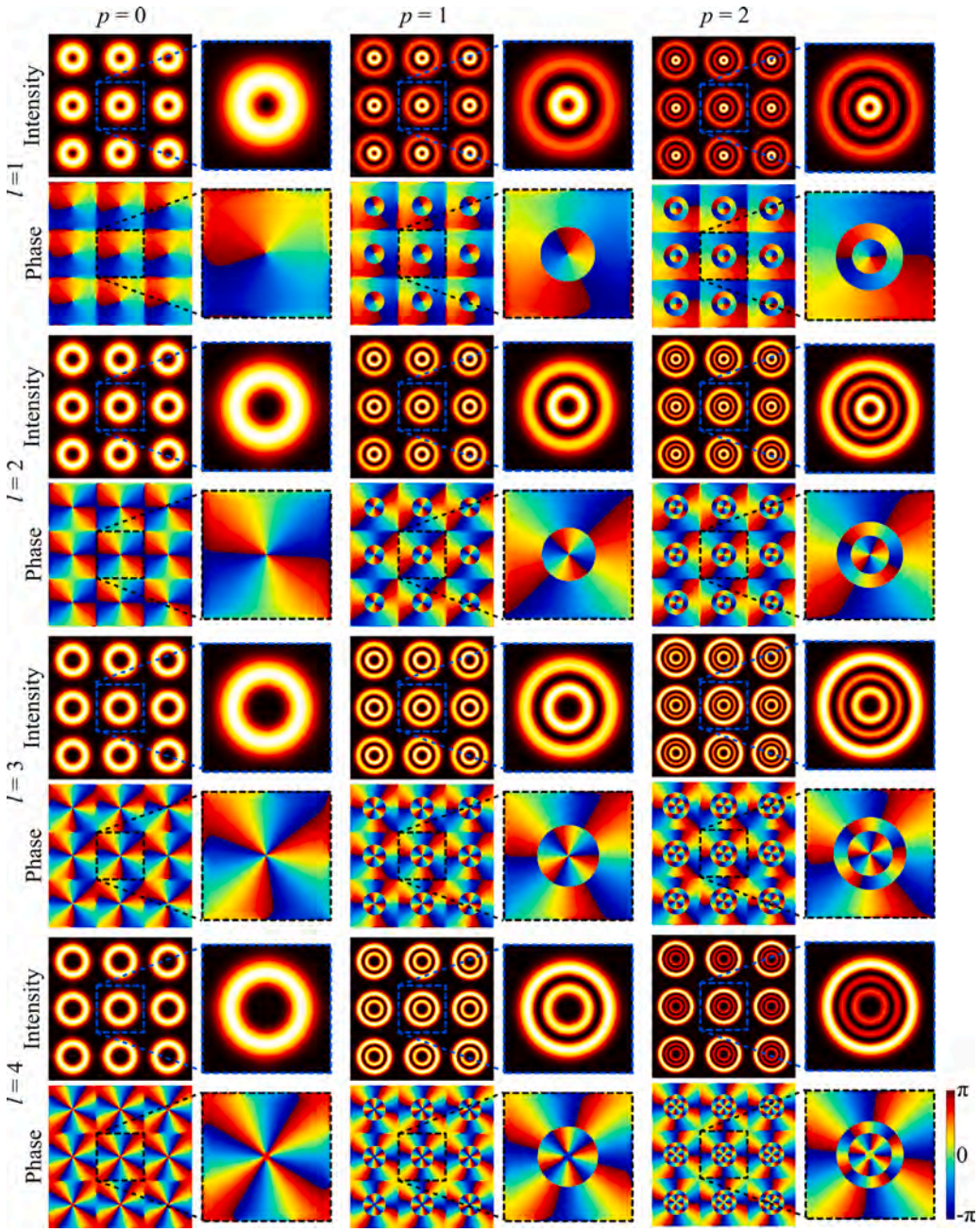

Fig. 7. Multiplication of LG beams with different values of TC and radial index in the ζ_{opt}. All parameters are the same as those in Fig. 5. See also Visualization 1.

offers a robust and versatile tool for advancing research and technology in optical sciences and beyond. For instance, when a 2D grating is used such that the incident beam strikes it perpendicularly from the top or bottom, and a glass cell containing a liquid with suspended particles is placed parallel to the grating plane at one of the optimal Talbot planes, each beam in the array can act as a 3D trap (as shown below). This setup makes it possible to trap and rotate suspended particles within the Talbot planes, enabling multi-particle trapping without the need for complex devices like SLMs and focusing systems.

In the optical communications context, we propose that each generated LG beam of an array can be coupled into an optical fiber, allowing for parallel communication channels. To demonstrate this option, we conducted simulations by isolating a single LG beam from the array using an obstacle with a circular aperture, as illustrated in Fig. 11. Fig. 11(a) shows the generated array of LG beams in the fourth Talbot plane. Fig. 11(b) depicts the obstacle used to isolate a single LG beam. Fig. 11(c) show the single LG beam passing through the circular aperture. Fig. 11(d), (e), and the inset presented as 11(f) demonstrate that the isolated LG beam propagates without distortion when other beams are absent. In Fig. 11(d) the divergence angles of the intensity rings are presented with $\theta_1 \approx 0.16°$ and $\theta_2 \approx 0.52°$. The inset in 11(f) implies that each beam creates a 3D trap in the vicinity of the Talbot planes. Additionally, other parts of Fig. 11 show the intensity and phase patterns of the propagated single LG beam at two different propagation distances. These results indicate that each generated beam in the array retains the proper characteristics of an LG beam, including the same intensity rings and phase profiles as the incident beam, albeit at a reduced size. This property facilitates their integration into an array of optical fibers for various applications.

In the following section, we present experimental results related to the generation of an array of LG beams. We display the intensity patterns observed at various Talbot and half-Talbot distances and compare

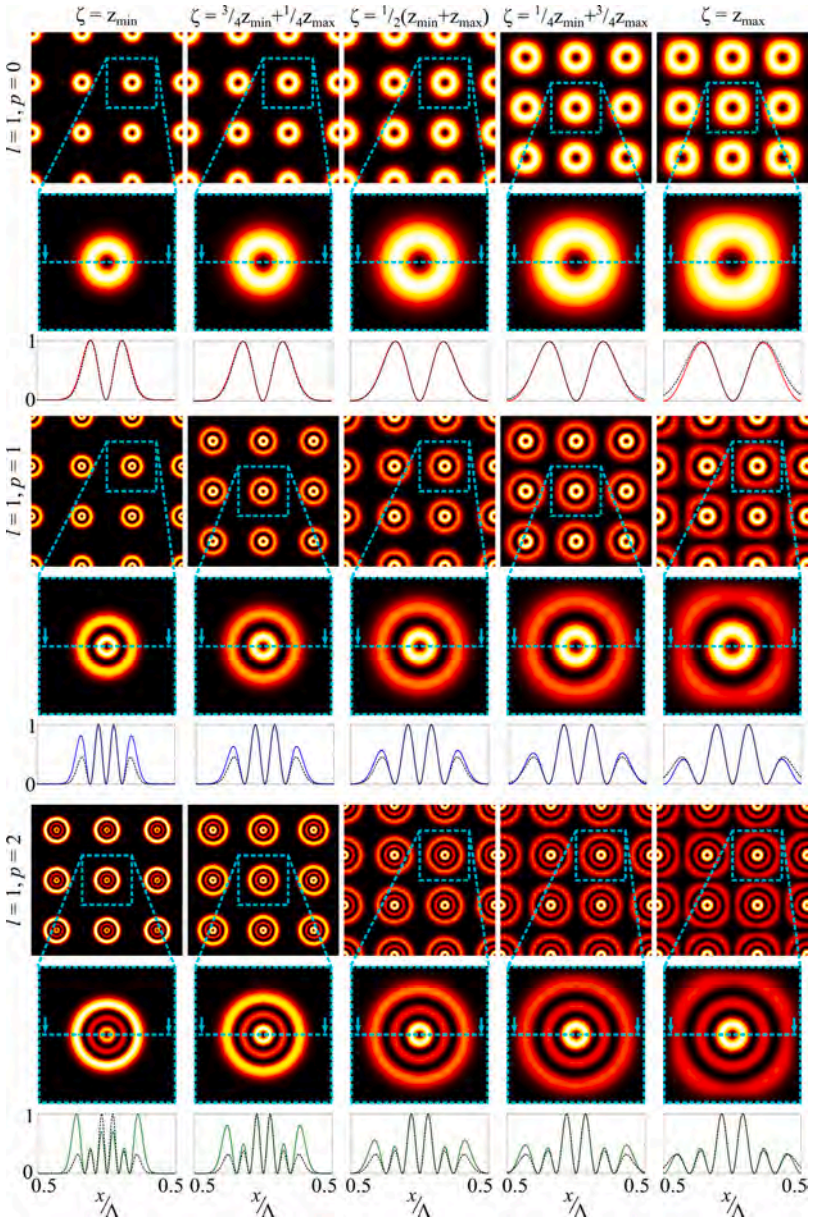

Fig. 8. First, fourth, and seventh rows, the intensity patterns of nine central lobes of LG modes realized by diffraction of specified LG beams from the same grating as in Fig. 5. The intensity profiles along the dashed line on each individually generated pattern and those of the corresponding incident LG beams are plotted in the third, sixth, and ninth rows with solid and dashed lines, respectively.

these experimental findings with the theoretical predictions discussed earlier. This comparison is intended to validate the theoretical models and establish a clear connection between theory and experiment.

5. Experiments and comparison of theoretical and experimental results

We exhibit the schematics of our experimental setup in Fig. 12. We transmit a collimated Gaussian beam from a neodymium-doped yttrium aluminum garnet (Nd:YAG) diode-pumped laser of carrier wavelength $\lambda = 532$ nm through a specially prepared amplitude fork grating to produce an LG beam with adjustable azimuthal and radial indices (l and p). These LG beams can also be generated using an SLM by implementing the same grating structures on the SLM. In this study, we present results based on amplitude fork gratings. For comparison, we also generated the same LG beams using an SLM (3M X50, resolution: 1024 × 768, display: 0.7 in, polysilicon LCD). Both methods produced beams with the same structure and quality, but the power share for the amplitude grating-based LG beams was higher. Therefore, we used these beams for the remainder of the work.

Due to intrinsic 2D periodicity of SLM structures, SLM functions almost as a 2D orthogonal binary structure. This leads to the generation of an array of incident beams rather than a single beam in the far-field, resulting in a lower power share for each diffraction order with unequal distribution among different orders. By implementing a fork grating on the SLM, each of the SLM diffraction orders branches into LG beams on the secondary non-zero diffraction orders, but with a much lower power share (see [4,41]). Employing amplitude fork gratings for the generation of LG beams eliminates the need for an SLM. Although the SLM facilitates precise control over the optical properties of beams, its diffraction efficiency is compromised by the intrinsic attributes of the 2D periodic structure. Furthermore, the SLM implementation increases the cost and complexity of the experimental protocol, requiring computer systems for its operation. In contrast, amplitude fork gratings

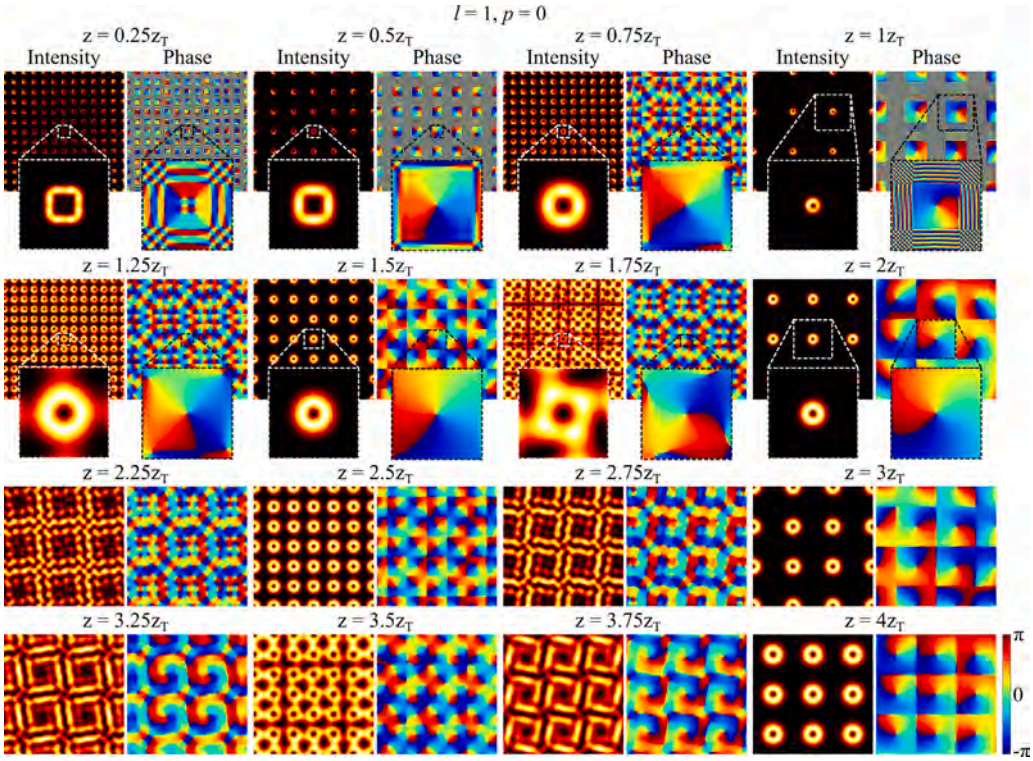

Fig. 9. Intensity and phase patterns in front of the nine central apertures of the grating under LG beam illumination with $l = 1$ and $p = 0$. The patterns are observed at various Talbot distances: full Talbot ($z = 2z_T$ and $z = 4z_T$), half-Talbot ($z = z_T$ and $z = 3z_T$), quarter-Talbot ($z = 0.5z_T$, $z = 1.5z_T$, $z = 2.5z_T$, and $z = 3.5z_T$), and octant-Talbot ($z = 0.25z_T$, $z = 0.75z_T$, $z = 1.25z_T$, $z = 1.75z_T$, $z = 2.25z_T$, $z = 2.75z_T$, $z = 3.25z_T$, and $z = 3.75z_T$). Here, $z_T = \frac{A^2}{\lambda}$. Other parameters for the beam and grating are the same as in Fig. 5.

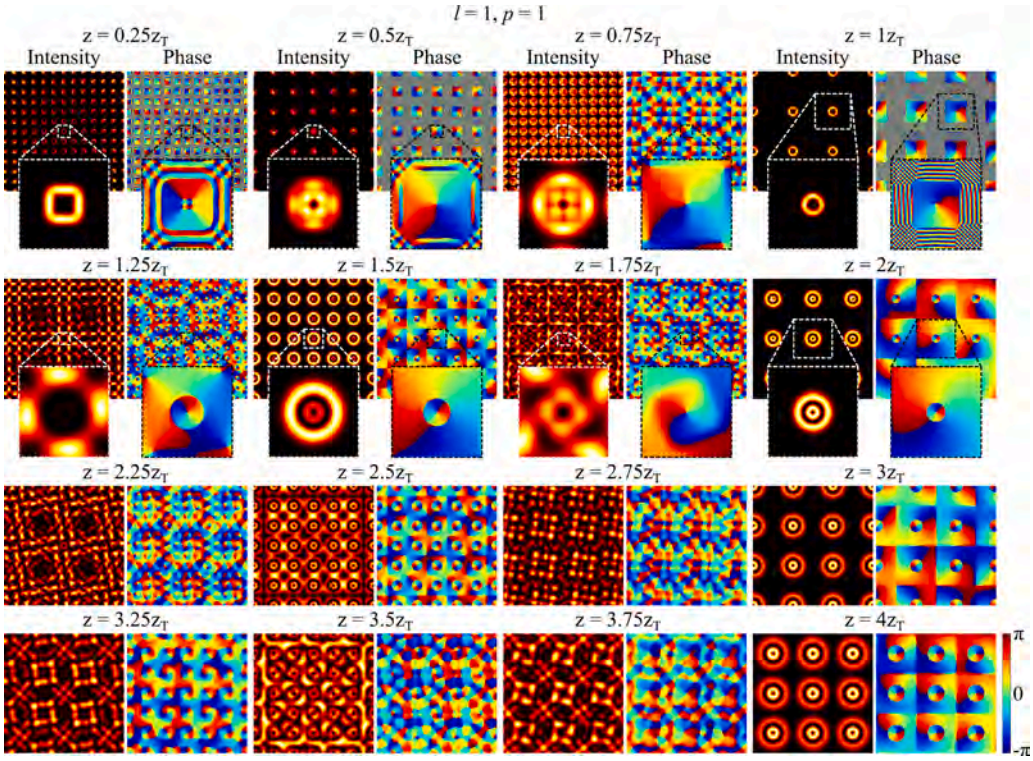

Fig. 10. The same intensity and phase patterns of Fig. 9 for an incident LG beam with $l = 1$ and $p = 1$.

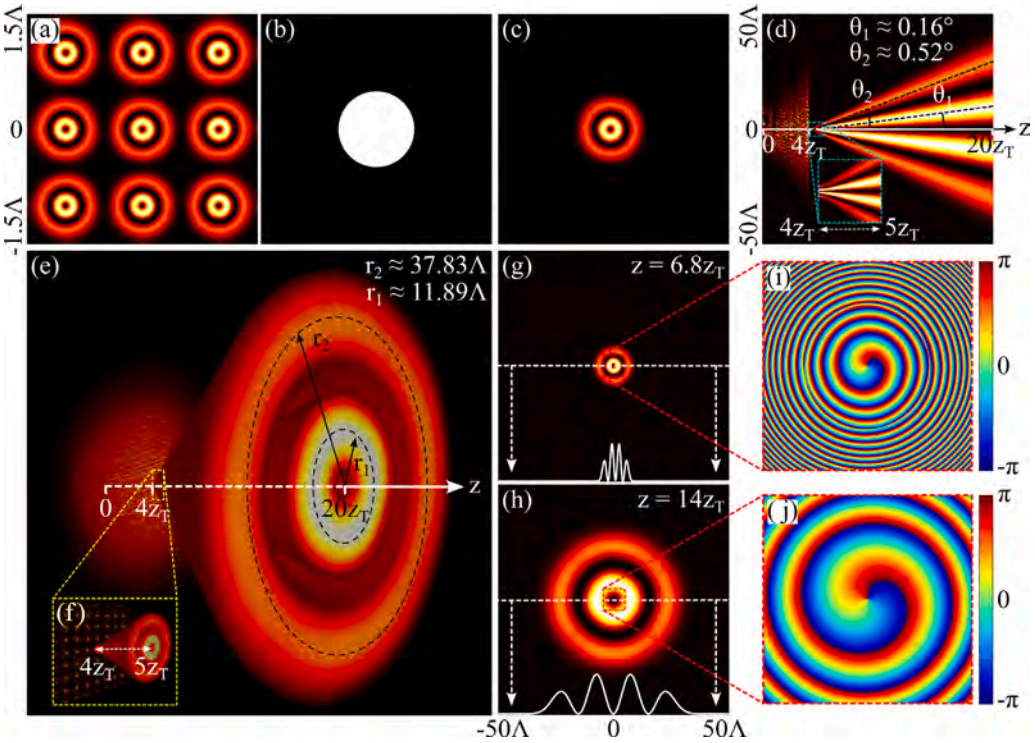

Fig. 11. Simulation demonstrating the feasibility of directing each generated LG beam of an array into an optical fiber for parallel communication channels. (a) The generated array of LG beams at the fourth Talbot plane. (b) The obstacle used to isolate a single LG beam at the fourth Talbot plane. (c) The single LG beam passing through the circular aperture. (d), (e), and the inset (f) show the isolated LG beam propagating without distortion when other beams are absent. (g) and (h) display the intensity, while (i) and (j) present the corresponding phase patterns of the propagated single LG beam at propagation distances of $z = 6.8z_T$ and $z = 14z_T$, respectively. In panel (e), $r_1 = 11.89\Lambda$ and $r_2 = 37.83\Lambda$ denote the radii of the first and second intensity rings at a propagation distance of $z = 20z_T$.

offer a straightforward and cost-effective approach to vortex beam generation, circumventing the complexities associated with SLMs.

As illustrated in Fig. 12, we allowed the generated LG beams to diffract from a 2D grating, producing arrays of LG beams with the same l and p indices as the incident LG beam in certain Talbot and Half-Talbot planes. To generate the required incident LG beams, we designed and constructed amplitude fork gratings with a specified dislocation number at the grating center, corresponding to the winding number or TC of the LG beam generated by the diffraction of the incident Gaussian beam. Additionally, we included a number of radii from the center of the grating where the lines have half-period displacements, corresponding to the number of intensity null rings in the generated LG beam, known as the p parameter. We printed the transmission functions of these gratings onto sheet glass.

It is important to understand how we utilize 1D fork gratings to generate LG beams with various l and p indices. Each of these generated beams was subsequently used to illuminate a 2D grating structure, resulting in a 2D array of incident beam replicas. In Appendix B, we present, a detailed design of generalized fork amplitude gratings. These gratings feature co-centered circular paths that share the same center as the fork grating. On these paths, we implemented specific lateral displacements on the grating lines, referred to as phase-shifted areas. We refer to these fork gratings, which have phase steps on certain co-centered circular paths, as 'multi-circle phase-shifted fork gratings' and 'generalized fork gratings'. The amplitude fork grating technique simplifies the generation of VBs, making it cost-effective and user-friendly. In contrast, the SLM based technique offers the advantage of easy adjustment of the VBs' characteristics.

We present a typical fork grating pattern, which can be directly printed on sheet glass or implemented on the SLM in a transmission mode, in the insets of the figure panel. The generated LG beams are then characterized using diffraction from a curved-line linear grating, confirming our method's efficacy (see [42] for details). Subsequently, the LG beam is transmitted through a 2D linear amplitude grating with a binary profile, having a period of 0.15 mm and an OR of 0.1. This grating is fabricated by coating its transmission function onto sheet glass. Lastly, we capture the near-field diffracted pattern with our camera (Nikon D7200). To ensure a high-resolution, aberration-free images, we record diffraction patterns directly onto the camera sensor, bypassing the imaging lens of the camera. We also installed the camera on a holder that can be precisely positioned on a rail to reach the camera's sensitive area in the half-Talbot and Talbot planes, determined by $z_T = \frac{\Lambda^2}{\lambda}$ and its odd multiples, and $z = 2z_T$ and its multiples, respectively. For the 2D grating used, with $\Lambda = 0.15$ mm and a laser beam wavelength of 532 nm, we have $z_T = 42$ mm.

We compare our experimental findings the theory, see red (theoretical) and green (experimental) patterns in Figs. 13 to 15. We observe good agreement between the two sets of results. Figs. 13 to 15 illustrate the generation of impinging LG beams through diffraction of a Gaussian beam by the amplitude fork gratings that are etched onto a glass sheet with a periodicity of 0.1 mm. Impinging LG beams are also synthesized using the SLM. However, we focus on those obtained with the aid of amplitude fork gratings due to their high intensity efficiency. The diffraction patterns presented in Figs. 13 and 14 were recorded in the corresponding ζ_{opt} planes. In Fig. 15, in addition to the diffraction patterns recorded in the optimal half-Talbot and Talbot planes between ζ_{min} and ζ_{max}, we have also included experimental and corresponding theoretical results for certain non-optimal half-Talbot and Talbot planes. This addition illustrates how, at the specified non-optimal half-Talbot distances (e.g., $z = 3z_T$ for $l = 2$ and $p = 1$, and $z = 5z_T$ for $l = 2$ and $p = 2$) and non-optimal Talbot distances (e.g., $z = 4z_T$ for $l = 2$ and $p = 2$), both the recorded experimental results and the predicted theoretical results exhibit low quality in the production of incident LG beam arrays. Additionally, moving away from the optimal planes results in the absence of incident LG beam arrays. The experimental outcomes, particularly those illustrated in the

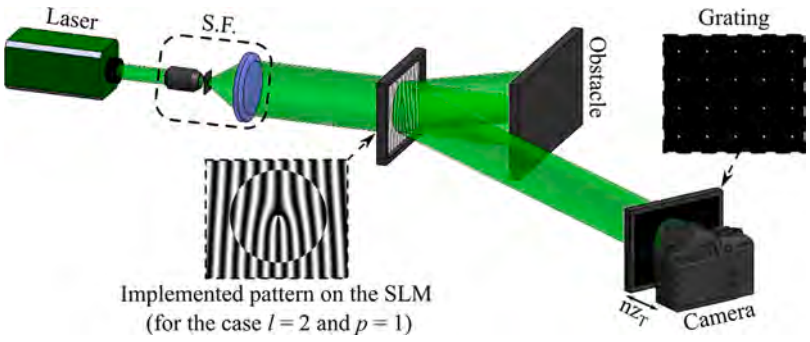

Fig. 12. Experimental setup for multiplication of LG beams with non-zero l and p parameters in certain Talbot planes. S.F. and z_T stand for spatial filter and Talbot distance, respectively; n is an integer.

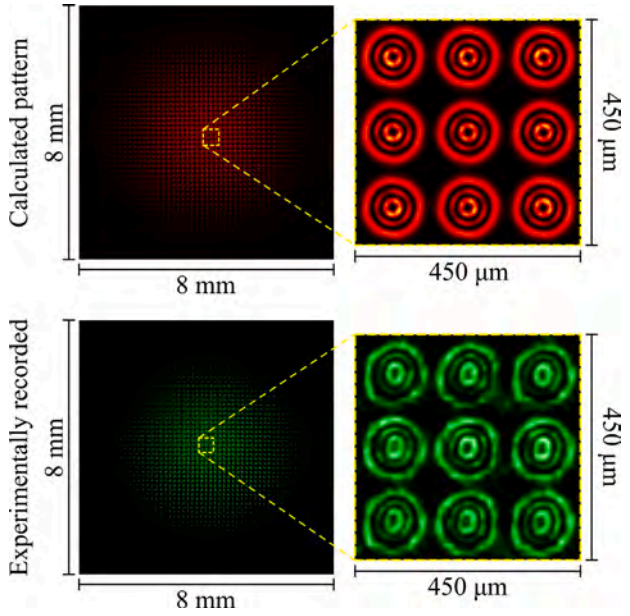

Fig. 13. Theoretical (red) and experimentally recorded (green) diffraction patterns observed in front of nine adjacent and central apertures of a 2D binary amplitude grating with an OR = 0.1 at the ζ_{opt} plane. The grating is illuminated by LG beams with $l = 0, \ldots, 4$ and $p = 0, 1, 2$. For all patterns, the 2D grating period and beam wavelength are $\Lambda = 0.15$ mm and $\lambda = 532$ nm, respectively. The generated LG beams have a beam width of $w_0 = 6\Lambda$. Optimal widths ranging from $w_{in}^G = 0.9 \pm 0.1$ mm to $w_{in}^G = 2.6 \pm 0.1$ mm were used for the Gaussian beam illuminating the amplitude fork gratings to ensure high-quality LG beams.

enlarged Fig. 13, are promising. The intensity of a central ring notably exceeds that of the secondary and tertiary ones, in accord with our theoretical predictions. Additionally, the third ring exhibits a wider intensity distribution in both the predicted and observed patterns. It is also noteworthy that the continuity of the second intensity loops is disrupted, which is consistent with theory and experiment.

6. Conclusions

We have theoretically explored the diffraction of LG beams with non-zero radial indices from a 2D binary grating with sufficiently small OR. We have elucidated the detailed structure of diffraction patterns in the near-field regime. In particular, we have shown that in certain Talbot planes, the image of each individual aperture of the grating has the same intensity pattern as an illuminating LG beam, thereby realizing efficient LG beam multiplication. The key to the success of our approach is to impose a reasonable limit on the radial extension of the replica LG beams, such that the multiplication interval can be defined over which the radial extension of each replica beam does not exceed the grating cell area Λ^2. This condition ensures that the multiplied LG beams do not overlap. We have identified an optimal propagation distance, z_{opt} over which the generated and incident beams have the maximum similarity with no overlap. We have shown that z_{opt} is very close to $z_{\max} = \zeta_{\max} z_T$, especially for the higher values of p.

Our method carries the potential for applications to OAM assisted optical information processing, as well as optical routing/switching in telecommunications. For example, our method can facilitate multi-particle manipulation and optical tweezers at different depths, corresponding to different Talbot planes in a sample. However, the main technical challenge of generating a high-power incident LG beam is yet to be addressed. The quality of the generated replicas of the incident LG beam depends on the 2D grating precision, including the parallelism of its lines and the uniformity of its opening ratio across all areas. Therefore, it is essential to print the grating on an optical glass substrate using optical lithography to ensure accuracy in applications. Additionally, imperfect LG beam illumination of a 2D grating can negatively impact the array generation. The Talbot effect entails ideal replication for incident Fourier-invariant waveforms, such as LG beams. Therefore, it is crucial to generate high-quality LG beams before multiplying them in Talbot planes.

CRediT authorship contribution statement

Pouria Amiri: Visualization, Software, Methodology, Data curation. **Saifollah Rasouli:** Writing – review & editing, Writing – original draft, Visualization, Validation, Supervision, Resources, Project administration, Methodology, Investigation, Funding acquisition, Formal analysis, Data curation, Conceptualization. **Davud Hebri:** Writing – review & editing, Writing – original draft, Visualization, Software, Methodology, Investigation, Formal analysis. **Sergey A. Ponomarenko:** Writing – review & editing, Validation, Investigation.

Funding

Institute for Advanced Studies in Basic Sciences, Iran (G2023IASBS12632), Center for International Scientific Studies and Collaboration (CISSC) of Iran (No. 4020667), Iran National Science Foundation, Iran (4020609), Natural Sciences & Engineering Research Council (NSERC) of Canada (RGPIN-2018-05497).

Declaration of competing interest

The authors declare that they have no competing interests.

Acknowledgments

This work is funded by the Institute for Advanced Studies in Basic Sciences (No. G2023IASBS12632), Center for International Scientific Studies and Collaboration (CISSC) of Iran (No. 4020667), Iran National Science Foundation (No. 4020609), and Natural Sciences & Engineering Research Council (NSERC) of Canada (No. RGPIN-2018-05497).

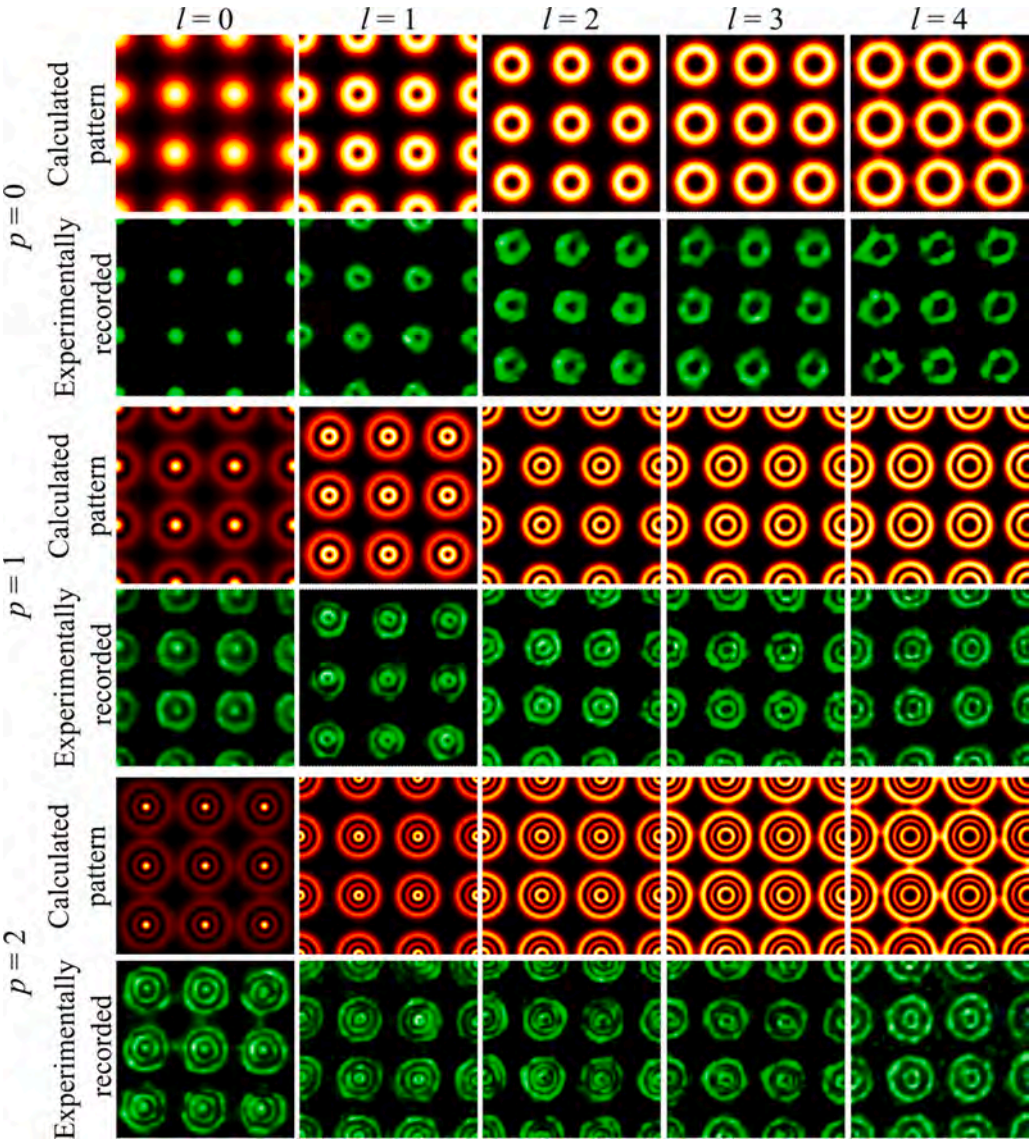

Fig. 14. Theoretical (red) and experimentally recorded (green) diffraction patterns in front of nine adjacent and central apertures of an amplitude 2D binary grating having an OR = 0.1 at ζ_{opt} plane when the grating is illuminated by LG beams with l =0, …,4 and p = 0, 1, 2. For all patterns, the 2D grating period and the beam wavelength were Λ = 0.15 mm and λ = 532 nm, respectively. For the generated LG beams a beam width of $w_0 = 6\Lambda$ is considered. Optimal widthes between $w_{in}^G = 0.9 \pm 0.1$ mm to $w_{in}^G = 2.6 \pm 0.1$ mm were used for the Gaussian beam illuminating the amplitude fork gratings to ensure high-quality LG beams.

Appendix A. Angular spectrum of LG beam

The complex amplitude of an LG beam in polar coordinates (r, θ) at the source plane $z = 0$ reads [39]

$$u_p^l(r,\theta) = \left(\frac{r}{w_0}\right)^{|l|} L_p^{|l|}\left(\frac{2r^2}{w_0^2}\right) \exp\left(-\frac{r^2}{w_0^2} + il\theta\right), \tag{A.1}$$

implying the following intensity profile:

$$I = R^{2|l|} \exp\left(-2R^2\right) \left[L_p^{|l|}\left(2R^2\right)\right]^2. \tag{A.2}$$

Here $R = \frac{r}{w_0}$ is a dimensionless radial parameter. As is well-known, the LG intensity profile includes $p+1$ concentric rings [39]. We define two radial parameters, called inner and outer radii, to characterize the radial extension of the LG beam. The inner and outer radii, w_{in} and w_{out}, can be defined as the shortest and longest radial distances from the optical axis of the beam at which the intensity falls to $\frac{1}{10}$ of its maximum value.

Next, a Fourier transform of an axially symmetric function $u(r,\theta) = f(r)\exp(il\theta)$ can be expressed as [38]:

$$U(\rho,\varphi) = 2\pi(-i)^{|l|} e^{il\varphi} \int_0^\infty f(r) J_{|l|}(2\pi r\rho) r dr, \tag{A.3}$$

where (ρ, φ) are the polar coordinates in the reciprocal space and we employed the property of Bessel function, $J_{-m} = (-1)^m J_m(x)$ [43]. It follows that

$$U_p^l(\rho,\varphi) = 2\pi w_0^2 (-i)^{|l|} e^{il\varphi} \int_0^\infty R^{|l|+1} L_p^{|l|}\left(2R^2\right) e^{-R^2} J_{|l|}\left(2\pi w_0 R\rho\right) d R. \tag{A.4}$$

Using the following table integral [44]:

$$\int_0^\infty x^{v+1} e^{-x^2} L_n^v\left(2x^2\right) J_v(xy) dx = \frac{(-1)^n}{2^{v+1}} y^v e^{-\frac{y^2}{4}} L_n^v\left(\frac{y^2}{2}\right), \tag{A.5}$$

we arrive at

$$U_p^l(\rho,\varphi) = \frac{\pi w^2 (-1)^p}{i^{|l|}} \left(\frac{\rho}{\rho_0}\right)^{|l|} L_p^{|l|}\left(\frac{2\rho^2}{\rho_0^2}\right) \exp\left(-\frac{\rho^2}{\rho_0^2} + il\varphi\right). \tag{A.6}$$

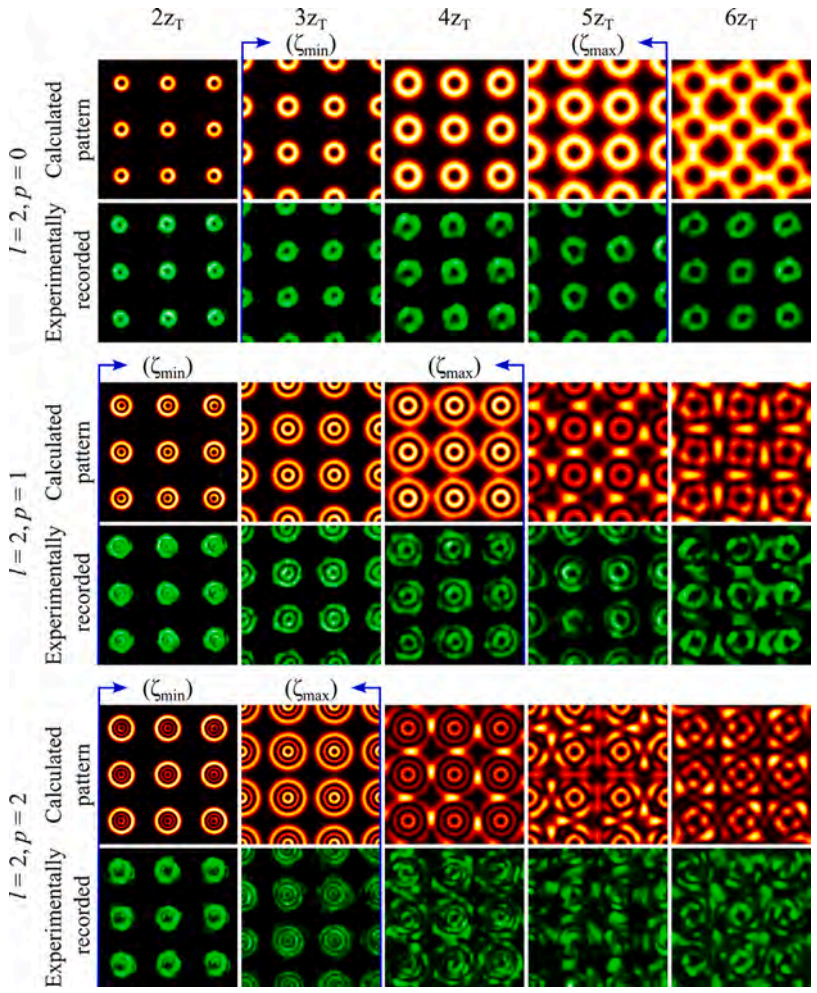

Fig. 15. Theoretical (red) and experimentally recorded (green) diffraction patterns at the optimal half-Talbot and Talbot planes between ζ_{min} and ζ_{max}, and in non-optimal half-Talbot and Talbot planes upon diffraction of an LG beam with variable l and p by an amplitude 2D binary grating with $\mu = 0.1$ and $\Lambda = 0.15$ mm. The other parameters are the same as in Fig. 14. At the specified non-optimal half-Talbot distances (e.g., $z = 3z_T$ for $l = 2$ and $p = 1$, and $z = 5z_T$ for $l = 2$ and $p = 2$) and non-optimal Talbot distances (e.g., $z = 4z_T$ for $l = 2$ and $p = 2$), both the recorded experimental results and the predicted theoretical results exhibit low quality in the production of incident LG beam arrays. Additionally, moving away from the optimal planes results in the absence of incident LG beam arrays.

Here $\rho_0 = \frac{1}{\pi w_0}$. On comparing Eqs. (A.6) and (A.1), we observe that LG beam profiles are self-Fourier transforms. We can then determine the radial extension in the reciprocal space as $\rho_{out} = R_{out}\rho_0 = \frac{R_{out}}{\pi w_0}$ where R_{out} is a dimensionless parameter illustrated in Fig. 1(e). Therefore, the angular spectrum bandwidth $\Delta\nu$ (transverse extension in the reciprocal space) can be expressed as

$$\Delta\nu = \frac{2R_{out}}{\pi w_0}. \tag{A.7}$$

Appendix B. Generation of LG beams with non-zero radial indices via diffraction of a Gaussian beam through multi-circle phase-shifted fork gratings

This appendix details the design of specialized fork gratings used to generate LG beams with non-zero radial indices by diffraction a Gaussian beam through them. These gratings, referred to as multi-circle phase-shifted fork gratings, consist of circular paths centered at a common points. Half-period lateral displacements are implemented on the grating lines, creating abrupt changes known as π-phase-shifted areas (see Fig. B.16).

The radii of the phase-shifted circles are determined based on the radii of the dark rings in the intensity pattern of the desired LG beam. For all the patterns depicted in Fig. B.16, based on the values of l and p of the desired LG beams, the radii of the phase-shifted circles are chosen such that all the resulting LG beams have the same parameter w_0 as described in Eq. (6).

To illustrate the details of the fork gratings both at the center and in the phase-shifted areas, we considered a period of 0.5 mm for all gratings. However, in the experiments, we used pure amplitude gratings with 10 lines/mm.

To generate LG beams with varying l and p parameters while maintaining the same w_0 parameter as shown in Eq. (6), we adjusted the beam width of the incident Gaussian beam, w_{in}^G, based on empirical observations.

In this study, we utilized multi-circle π-phase-shifted fork gratings to transform a Gaussian beam into LG beams characterized by a radial index p and a TC l. For each p value, the beam's radial profile exhibits $p + 2$ radial nodes where the light intensity is zero: one on the optical axis ($r = 0$), one at infinity ($r = \infty$), and p intensity nodes located at intermediate radial distances. This means there are $p+1$ intensity rings for the generated LG beam.

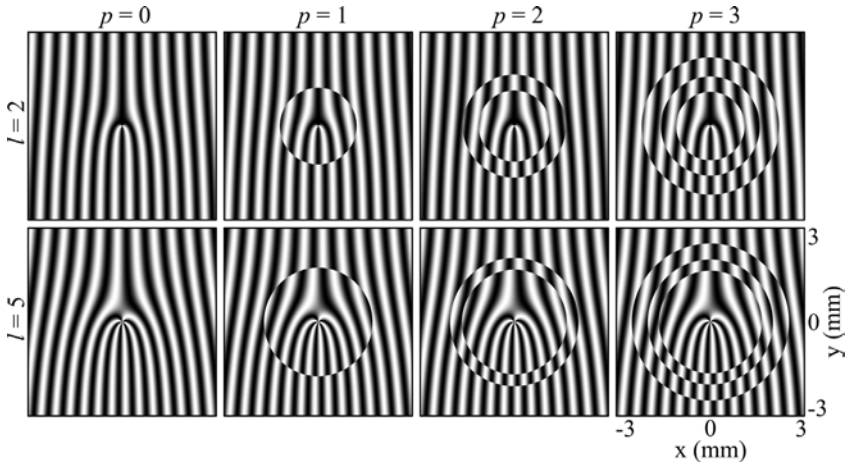

Fig. B.16. Transmittances of various multi-circle phase-shifted fork gratings with sinusoidal profiles, characterized by central and intermediate radial phase discontinuities defined by the parameters l and p, respectively. Each grating has dimensions of $3\,\text{mm} \times 3\,\text{mm}$ with a grating period of $d = 0.5\,\text{mm}$. These gratings are designed for LG beams with a width of $w_0 = 0.5\,\text{mm}$.

Table B.1
Values of $r_k^{(l,p)}$ for $l = 2$ and $l = 5$ with $p = 1$ to $p = 3$.

$l = 2$		
$p = 1$	$p = 2$	$p = 3$
$r_1^{(2,1)} = \frac{\sqrt{6}}{2} w_0$	$r_1^{(2,2)} = 1 w_0$	$r_1^{(2,3)} \approx 0.87 w_0$
–	$r_2^{(2,2)} = \sqrt{3} w_0$	$r_2^{(2,3)} \approx 1.47 w_0$
–	–	$r_3^{(2,3)} \approx 2.14 w_0$
$l = 5$		
$p = 1$	$p = 2$	$p = 3$
$r_1^{(5,1)} = \sqrt{3} w_0$	$r_1^{(5,2)} \approx 1.48 w_0$	$r_1^{(5,3)} \approx 1.32 w_0$
–	$r_2^{(5,2)} \approx 2.20 w_0$	$r_2^{(5,3)} \approx 1.91 w_0$
–	–	$r_3^{(5,3)} \approx 2.57 w_0$

At the optical axis, there is a phase singularity due to the fork form of the grating, causing an intensity node there. The intensity node at $r = \infty$ originates from the exponentially decreasing amplitude feature of the Gaussian beam at large radii.

At the location of each intermediate node, a π phase shift for the fork grating lines is implemented to achieve the desired LG beam pattern with $p + 1$ intensity rings. For instance, we have the following conditions:

- When $p = 0$, there are no intermediate radial nodes, resulting in a simple forked grating.
- For $p = 1$, an intermediate radial node appears at $r_1^{(l,1)} = w_0\sqrt{\frac{|l|+1}{2}}$, requiring a phase difference of π between the inner and outer radii of $r_1^{(l,1)} = w_0\sqrt{\frac{|l|+1}{2}}$.
- For $p = 2$, two intermediate radial nodes are present at $r_1^{(l,2)} = w_0\sqrt{\frac{|l|+2-\sqrt{|l|+2}}{2}}$ and $r_2^{(l,2)} = w_0\sqrt{\frac{|l|+2+\sqrt{|l|+2}}{2}}$, with phase differences of π and 2π, respectively.

In the general case for radial index p and TC l, the radial nodes $r_k^{(l,p)}$ ($k = 1, 2, \ldots, p$) are derived from the zeros of the Laguerre polynomials presented in Eq. (6). Table B.1 presents typical values of $r_k^{(l,p)}$ for various l and p indices, expressed in terms of the width parameter w_0 of the desired LG beam. At nodes radii, a phase difference of $(k\pi)$ must be applied, where k denotes the intermediate node ring number. Thus, a general relationship for the used multi-circle phase-shifted fork gratings is expressed as follows:

$$t(x,y) = 0.5\left(1 + \cos\left(\frac{2\pi}{d}x + l\theta + \Delta\phi(r)\right)\right),$$

$$\Delta\phi(r) = \begin{cases} 0, & \text{if } p = 0, \\ \begin{cases} 0, & \text{if } r < r_1^{(l,1)} \\ \pi, & \text{if } r \geq r_1^{(l,1)}, \end{cases} & \text{if } p = 1, \\ \begin{cases} 0, & \text{if } r < r_1^{(l,2)} \\ \pi, & \text{if } r_1^{(l,2)} \leq r < r_2^{(l,2)} \\ 2\pi, & \text{if } r \geq r_2^{(l,2)}, \end{cases} & \text{if } p = 2, \\ \vdots \end{cases} \tag{B.1}$$

where d is the period in the x-direction. The parameter l, representing the dislocation number at the grating center, corresponds to the winding number or TC of the LG beam generated by the diffraction of the incident Gaussian beam through the fork grating. The variable θ denotes the azimuth direction.

Appendix C. Supplementary data

See Supplement 1 for supporting content.

Supplementary material related to this article can be found online at https://doi.org/10.1016/j.optcom.2024.131203.

Data availability

No data was used for the research described in the article.

References

[1] X. Wang, Z. Nie, Y. Liang, J. Wang, T. Li, B. Jia, Recent advances on optical vortex generation, Nanophotonics 7 (9) (2018) 1533–1556.
[2] G.-X. Wei, L.-L. Lu, C.-S. Guo, Generation of optical vortex array based on the fractional Talbot effect, Opt. Commun. 282 (14) (2009) 2665–2669.
[3] J. Bayat, F. Hajizadeh, A.M. Khazaei, S. Rasouli, Gear-like rotatable optical trapping with radial carpet beams, Sci. Rep. 10 (1) (2020) 11721.
[4] P.Y. Moghadam, S. Rasouli, F. Hajizadeh, D. Hebri, Three-dimensional optical multiple trapping using pure amplitude octagonal almost periodic structures, Opt. Express 31 (26) (2023) 43490–43505.

[5] K. Toyoda, K. Miyamoto, N. Aoki, R. Morita, T. Omatsu, Using optical vortex to control the chirality of twisted metal nanostructures, Nano Lett. 12 (7) (2012) 3645–3649.
[6] M. Woerdemann, C. Alpmann, M. Esseling, C. Denz, Advanced optical trapping by complex beam shaping, Laser Photonics Rev. 7 (6) (2013) 839–854.
[7] J. Wang, J.-Y. Yang, I.M. Fazal, N. Ahmed, Y. Yan, H. Huang, Y. Ren, Y. Yue, S. Dolinar, M. Tur, et al., Terabit free-space data transmission employing orbital angular momentum multiplexing, Nat. Photonics 6 (7) (2012) 488–496.
[8] G. Gibson, J. Courtial, M.J. Padgett, M. Vasnetsov, V. Pas'ko, S.M. Barnett, S. Franke-Arnold, Free-space information transfer using light beams carrying orbital angular momentum, Opt. Express 12 (22) (2004) 5448–5456.
[9] N. Bozinovic, Y. Yue, Y. Ren, M. Tur, P. Kristensen, H. Huang, A.E. Willner, S. Ramachandran, Terabit-scale orbital angular momentum mode division multiplexing in fibers, Science 340 (6140) (2013) 1545–1548.
[10] T. Lei, M. Zhang, Y. Li, P. Jia, G.N. Liu, X. Xu, Z. Li, C. Min, J. Lin, C. Yu, et al., Massive individual orbital angular momentum channels for multiplexing enabled by Dammann gratings, Light: Sci. Appl. 4 (3) (2015) e257.
[11] A.M. Khazaei, D. Hebri, S. Rasouli, Theory and generation of heterogeneous 2D arrays of optical vortices by using 2D fork-shaped gratings: topological charge and power sharing management, Opt. Express 31 (10) (2023) 16361–16379.
[12] L. Zhu, M. Tang, H. Li, Y. Tai, X. Li, Optical vortex lattice: an exploitation of orbital angular momentum, Nanophotonics 10 (9) (2021) 2487–2496.
[13] G. Ruffato, M. Massari, F. Romanato, Multiplication and division of the orbital angular momentum of light with diffractive transformation optics, Light: Sci. Appl. 8 (1) (2019) 113.
[14] T. Wang, V. Tran, P. Bassène, E. Fohtung, T. Rhone, M. N'Gom, Adaptive methods of generating complex light arrays, J. Opt. Soc. Amer. A 41 (1) (2024) 104–110.
[15] M. Bock, A. Treffer, R. Grunwald, Nondiffracting self-imaging of ultrashort wavepackets, Opt. Lett. 42 (12) (2017) 2374–2377.
[16] M. Liebmann, A. Treffer, M. Bock, T. Seiler, J. Jahns, T. Elsaesser, R. Grunwald, Self-imaging of tailored vortex pulse arrays and spectral Gouy rotation echoes, Opt. Lett. 44 (4) (2019) 1047–1050.
[17] S. Rasouli, D. Hebri, Theory of diffraction of vortex beams from 2D orthogonal periodic structures and Talbot self-healing under vortex beam illumination, J. Opt. Soc. Amer. A 36 (5) (2019) 800–808, http://dx.doi.org/10.1364/JOSAA.36.000800, URL https://opg.optica.org/josaa/abstract.cfm?URI=josaa-36-5-800.
[18] A. Dudley, A. Forbes, From stationary annular rings to rotating Bessel beams, J. Opt. Soc. Amer. A 29 (4) (2012) 567–573.
[19] X. Li, H. Zhang, Anomalous ring-connected optical vortex array, Opt. Express 28 (9) (2020) 13775–13785.
[20] L. Ma, S.A. Ponomarenko, Optical coherence gratings and lattices, Opt. Lett. 39 (23) (2014) 6656–6659.
[21] C. Liang, X. Liu, Z. Xu, F. Wang, W. Wen, S.A. Ponomarenko, Y. Cai, P. Ma, Perfect optical coherence lattices, Appl. Phys. Lett. 119 (13) (2021).
[22] L. Ma, S.A. Ponomarenko, Free-space propagation of optical coherence lattices and periodicity reciprocity, Opt. Express 23 (2) (2015) 1848–1856.
[23] C. Liang, X. Zhu, C. Mi, X. Peng, F. Wang, Y. Cai, S.A. Ponomarenko, High-quality partially coherent Bessel beam array generation, Opt. Lett. 43 (13) (2018) 3188–3191.
[24] C. Liang, C. Mi, F. Wang, C. Zhao, Y. Cai, S.A. Ponomarenko, Vector optical coherence lattices generating controllable far-field beam profiles, Opt. Express 25 (9) (2017) 9872–9885.
[25] D. Hebri, S. Rasouli, Theoretical study on the diffraction-based generation of a 2D orthogonal lattice of optical beams: physical bases and application for a vortex beam multiplication, J. Opt. Soc. Amer. A 39 (9) (2022) 1694–1711.
[26] B. Knyazev, O. Kameshkov, N. Vinokurov, V. Cherkassky, Y. Choporova, V. Pavelyev, Quasi-Talbot effect with vortex beams and formation of vortex beamlet arrays, Opt. Express 26 (11) (2018) 14174–14185.
[27] D.A. Ikonnikov, S.A. Myslivets, M.N. Volochaev, V.G. Arkhipkin, A.M. Vyunishev, Two-dimensional Talbot effect of the optical vortices and their spatial evolution, Sci. Rep. 10 (1) (2020) 20315.
[28] D.A. Ikonnikov, S.A. Myslivets, V.G. Arkhipkin, A.M. Vyunishev, 3D optical vortex lattices, Ann. Phys., Lpz. 533 (7) (2021) 2100114.
[29] J. Li, F. Li, K. Chen, L. Yu, X. Chen, X. Qian, J. Ma, C. Yuan, Vortex array generation based on Quasi-Talbot effects, J. Opt. Soc. Amer. A 40 (8) (2023) 1537–1544.
[30] P. Panthong, S. Srisuphaphon, A. Pattanaporkratana, S. Chiangga, S. Deachapunya, A study of optical vortices with the Talbot effect, J. Opt. 18 (3) (2016) 035602, http://dx.doi.org/10.1088/2040-8978/18/3/035602.
[31] P. Panthong, S. Srisuphaphon, S. Chiangga, S. Deachapunya, High-contrast optical vortex detection using the Talbot effect, Appl. Opt. 57 (7) (2018) 1657–1661, http://dx.doi.org/10.1364/AO.57.001657, URL https://opg.optica.org/ao/abstract.cfm?URI=ao-57-7-1657.
[32] S. Deachapunya, S. Srisuphaphon, S. Buathong, Production of orbital angular momentum states of optical vortex beams using a vortex half-wave retarder with double-pass configuration, Sci. Rep. 12 (1) (2020) 6061.
[33] S. Buathong, S. Srisuphaphon, S. Deachapunya, Probing vortex beams based on Talbot effect with two overlapping gratings, J. Opt. 24 (2) (2022) 025602, http://dx.doi.org/10.1088/2040-8986/ac477c.
[34] S. Rasouli, P. Amiri, D. Hebri, Transformation of Laguerre-Gaussian beams into 1D array of Hermite-Gaussian modes under the Talbot effect, Opt. Express 31 (13) (2023) 20683–20695.
[35] M. Yeganeh, S. Rasouli, M. Dashti, S. Slussarenko, E. Santamato, E. Karimi, Reconstructing the Poynting vector skew angle and wavefront of optical vortex beams via two-channel moiré deflectometery, Opt. Lett. 38 (6) (2013) 887–889, http://dx.doi.org/10.1364/OL.38.000887, URL https://opg.optica.org/ol/abstract.cfm?URI=ol-38-6-887.
[36] S. Rasouli, M. Yeganeh, Use of a two-channel moiré wavefront sensor for measuring topological charge sign of the vortex beam and investigation of its change due to an odd number of reflections, Int. J. Opt. Photonics 7 (2) (2013) 77–83.
[37] D. Hebri, S. Rasouli, Diffraction from two-dimensional orthogonal nonseparable periodic structures: Talbot distance dependence on the number theoretic properties of the structures, J. Opt. Soc. Amer. A 36 (2) (2019) 253–263.
[38] J.W. Goodman, Introduction to Fourier Optics, Roberts & Company, 2005.
[39] G.J. Gbur, Singular Optics, CRC Press, 2016.
[40] J.C. Yue, M.K. Clayton, A similarity measure based on species proportions, Commun. Stat.-Theory Methods 34 (11) (2005) 2123–2131.
[41] S. Rasouli, A.M. Khazaei, An azimuthally-modified linear phase grating: generation of varied radial carpet beams over different diffraction orders with controlled intensity sharing among the generated beams, Sci. Rep. 9 (1) (2019) 12472.
[42] S. Rasouli, S. Fathollazade, P. Amiri, Simple, efficient and reliable characterization of Laguerre-Gaussian beams with non-zero radial indices in diffraction from an amplitude parabolic-line linear grating, Opt. Express 29 (19) (2021) 29661–29675, http://dx.doi.org/10.1364/OE.435116, URL https://opg.optica.org/oe/abstract.cfm?URI=oe-29-19-29661.
[43] G.B. Arfken, H.J. Weber, Mathematical Methods for Physicists, American Association of physics teachers, 1999.
[44] I.S. Gradshteyn, I.M. Ryzhik, Table of Integrals, Series, and Products, Academic Press, 2014.